Design of High-Efficiency Inductive Charging System With Load-Independent Output Voltage and Current Tolerant of Varying Coupling Condition

Chi Shing Wong, *Member, IEEE*, Man-Chung Wong, *Senior Member, IEEE*, Lingling Cao, *Member, IEEE*, and K. H. Loo, *Member, IEEE*

***Abstract*—Maintaining constant-current (CC) and constant-voltage (CV) outputs for meeting the charging profile of lithium-ion batteries while realizing zero-voltage-switching on the primary bridge over wide ranges of load and coupling variations are rather challenging due to the presence of leakage and magnetizing inductances of a loosely coupled transformer. Although the challenges can be greatly relaxed by properly designing a compensation network with load-independent output characteristics, the desirable characteristics rendered by fixed compensation networks will be lost and cannot be fully restored by existing control methods once the designed compensation is deviated from the nominal coupling condition. In this article, a dynamic series/series–parallel compensation network, which originally aims to deliver constant output voltage only, is further investigated as a feasible topology for CC–CV battery charger adaptive to different sizes of air gap/misalignment of the coils. As benefited from the extra controllability offered by the parallel compensation capacitance as compared to the series/series compensation counterpart, this article provides alternative design criterion for the effective parallel compensation capacitance for designing and maintaining desirable charging currents in the CC stage while maximizing the efficiency in the CV stage under varying coupling condition. An experimental prototype with the air gap ranging from 10 to 16 cm is built to verify the idea.**

***Index Terms*—Battery charger, dynamic series/series–parallel (S/SP) compensation, inductive power transfer (IPT), switch-controlled capacitor (SCC), varying coupling condition.**

Manuscript received January 6, 2021; revised March 25, 2021; accepted May 28, 2021. Date of publication June 7, 2021; date of current version August 16, 2021. This work was supported by Hong Kong RGC Postdoctoral Fellowship Scheme 2020/21 under Project PDFS2021-5S10. Recommended for publication by Associate Editor M. Ponce-Silva. *(Corresponding author: Chi Shing Wong.)*

Chi Shing Wong is with the Department of Electronic, and Information Engineering, The Hong Kong Polytechnic University, Hong Kong (e-mail: chi.shing.wong@connect.polyu.hk).

Man-Chung Wong is with the Electrical and Computer Engineering, Faculty of Science and Technology, and the State Key Laboratory of Internet of Things for Smart City, University of Macau, Macau 999078, China (e-mail: mcwong@umac.mo).

Lingling Cao is with the School of Mechanical Engineering, and Automation, Harbin Institute of Technology, Shenzhen 518055, China (e-mail: caolingling@hit.edu.cn).

K. H. Loo is with the Department of Electronic and Information Engineering, The Hong Kong Polytechnic University, Hong Kong (e-mail: kh.loo@polyu.edu.hk).

Color versions of one or more figures in this article are available at https://doi.org/10.1109/TPEL.2021.3086858.

Digital Object Identifier 10.1109/TPEL.2021.3086858

I. Introduction

ELECTRIC power transfer between various sources and loads via sockets and cables is well existed since the advent of electricity in the 19th century [1]. However, owing to the advantages of wireless power transfer and the increasing popularity of mobile electric loads in the recent years, power transfer via magnetic link have been extensively investigated by academia and increasingly employed in various daily battery-charging applications from low to high power such as biomedical implant, portable electronic devices, and electric vehicles (EVs) [2]–[7]. Among various types of battery, lithium-ion (Li-ion) batteries are considered as one of the suitable candidates for the battery-powered applications due to their improved battery life and higher energy density [8]. Even though the electrical characteristics are varied from battery to battery, a standard and widely adopted charging protocol for Li-ion batteries is constant-current-constant-voltage (CC–CV) charging for which the battery pack is initially charged by constant-current (CC) and subsequently by constant-voltage (CV) as the terminal voltage reaches the prescribed value [8]. The charging process is ended when the charging current decays to the preset minimum. In general, the rate of a charging process is governed by the magnitude of the current in the CC stage [9]. In addition, variants of CC–CV charging strategies are proposed, which split the charging current into multiple stages to reduce the temperature rise and extend the battery cycle life [8]. Therefore, it is advantageous if the charging current can be flexibly fixed by the charger. Throughout the charging process, the battery equivalent resistance R_{bat} can vary from several ohms to hundreds ohms. As a result, it is challenging to maintain high efficiency and stable output voltage/current over wide range of load in the respective stage of a charging process.

In inductive-power-transfer (IPT) systems, the transmitter and receiver coils are separated by an air gap and can be placed freely in the designated area, leading to imperfect magnetic coupling, and hence, the leakage and magnetizing inductances are nonnegligible. Moreover, the variation of the inductances due to different sizes of air gap/misalignment can further deviate the output from the nominal value and introduce significant reactive power under different load resistances and coupling conditions [10]. Even though constant output voltage and current can be obtained by modulating the primary bridge voltage

without front-end or downstream dc–dc converter, the conditions for achieving zero-voltage-switching (ZVS) on the primary bridge is difficult to be maintained over the entire range of load due to the possible wide variation of duty cycle, resulting in electromagnetic interference issues, additional switching losses, and reliability problems [11]. Moreover, the associated reactive power and the fluctuating input impedance angle due to the presence of the inductances remain unsolved, which pose additional challenges for achieving high-power transfer efficiency and ZVS on the primary bridge under varying load and coupling conditions. Therefore, the design of compensation networks has become an important research topic in IPT systems for which the effects of the inductances of the loosely coupled transformer are suppressed by resonating the inductances with additional series or parallel capacitors. By doing so, the reactive power drawn by the primary bridge can be minimized by the resulting nearly resistive input impedance for improving power transfer capability. Meanwhile, a load-independent output voltage/current can be designed such that desirable output can be regulated without the need of large duty cycle variation, which greatly simplifies the realization of ZVS on the primary bridge for wide range of load variation [11].

In the past few years, a number of compensation networks have been proposed in the literature for achieving the objectives of load-independent outputs with resistive input impedance simultaneously. The earlier proposed compensation networks are based on two additional capacitors placed on both sides of the transformer, which form four basic compensation networks, namely series/series (S/S), series/parallel, parallel/series, and parallel/parallel compensations [12]. Unfortunately, the basic compensation networks can only achieve either CC or CV output with unity power factor under the designed coupling condition [13]. In order to deliver both CC and CV outputs with unity power factor for meeting the charging profile of battery, several hybrid compensation networks were proposed, which basically integrate two networks, which can individually give CC or CV output, with additional relays or bidirectional switches into a single IPT converter [13]–[16]. By switching between these two networks, CC and CV outputs can be achieved with unity power factor. However, this method requires high component count and, hence, increased cost and lower power density. Apart from the basic compensations with capacitors only, other higher order compensation networks involving additional inductors, such as *LC*/*LC* and *LCC*/*LCC* compensation networks were proposed for EV charging applications [17]–[19]. For *LC*/*LC* compensation network [17], only load-independent output current with unity power factor can be achieved. Later, an *LCC*/*LCC* compensation network with a new design approach was proposed, which not only deliver load-independent output current but also load-independent output voltage with unity power factor at two frequencies [19]. Nevertheless, the number of passive components used in higher order compensation networks is still comparable with hybrid compensation networks [20], [21]. Furthermore and most importantly, the designs of the compensation networks are heavily dependent on the leakage and/or the mutual inductance of the loosely coupled transformer. In other words, none of the fixed compensation networks can maintain the same magnitude of output voltage/current and the input impedance angle over wide range of coupling condition. Hence, the adverse effects of the loosely coupled transformer will become notable again under the displacement of the transmitter and receiver coils.

In order to regulate the output and retain the properties originally offered by the designed compensation network under the variation of coupling, additional control mechanisms must be implemented to deal with the resulting changes of transformer parameters. However, the conventional control methods could inadequately restore the nominal properties of the compensation network. Apart from the typical pulse-width-modulation of the primary bridge, which is straightforward but difficult to maintain ZVS operation for wide range of duty cycle variation, frequency-modulation is also common for output regulation or input impedance angle control of IPT systems [22]–[24]. In [23], a self-oscillating control of S/S compensated IPT converter is proposed, which can restore the property of load-independent output voltage under varying coupling condition by changing the operating frequency of the converter. However, the resulting input impedance angle for obtaining load-independent output voltage is inductive, which is irreducible and could cause excessive conduction loss. To minimize the excessive reactive power and ensure ZVS operation of the primary bridge, pulsewidth modulation in conjunction with variable frequency control is proposed for S/S compensation [25], [26]. Unfortunately, since the operating point of the network is shifted away from the load-independent output, the control loops need to keep track closely with the necessary voltage and current information in the transmitter- and receiver-ends and update the duty cycle and the frequency of the primary bridge. The implementation is computational-intensive and requires a reliable real-time wireless communication link.

As a derivative of the basic S/S compensation with only moderate increase in passive component count, series/series-parallel (S/SP) compensation is formed by adding an additional parallel compensation capacitor such that load-independent output voltage can be achieved while the input impedance is resistive due to the cancellation of the magnetizing inductance [27], [28]. However, similar to the other existing compensation networks, the existing control methods can only partially restore the designed characteristics of the network upon the change of coupling condition. To this end, by adding one more degree of control freedom other than duty cycle and switching frequency of the primary bridge, a dynamic S/SP compensation is recently proposed in [29] for which the parallel compensation capacitance can be adaptively varied under different coupling conditions by switch-controlled capacitor (SCC). Even though the application of SCC is drawing increasing attention in a few other compensation networks to achieving either load-independent output voltage or current in recent years [30]–[32], the capability to deliver both CC and CV outputs under varying coupling condition is yet to study in these networks.

In this article, the advantages and the characteristics of the dynamic S/SP compensation network will be further studied and fully exploited. Extending from the work in [29], which primarily provides load-independent output voltage with resistive input impedance by the network, this article further explores its

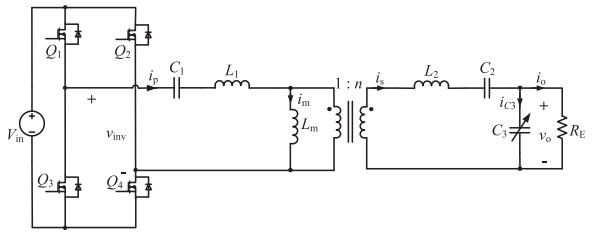

Fig. 1. Circuit diagram of the dynamic S/SP compensated IPT converter.

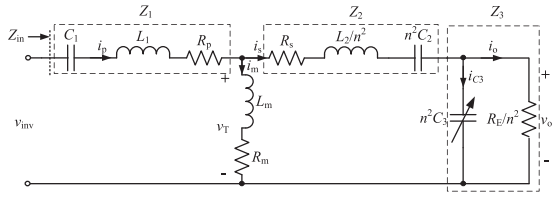

Fig. 2. Simplified circuit diagram of the dynamic S/SP compensation network with all circuit elements reflected to the primary side.

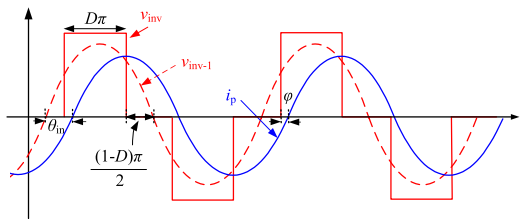

Fig. 3. Theoretical waveforms of the ZVS operation of the primary bridge.

potential to deliver load-independent output current simultaneously with the network such that an intact CC–CV battery charger with ZVS capability tolerant of different coupling conditions can be constructed. Also, given the extra controllability of the parallel compensation capacitance in the dynamic S/SP compensation as compared to the conventional S/S compensation network, the magnitude of the load-independent output current in the CC stage can be flexibly configured for meeting different charging requirements. Despite the advantages offered by the extra control degree of freedom with SCC, its impacts on the power transfer efficiencies in both CC and CV stages deserve a deeper investigation. Contrary to the general presumption of the design of compensation networks, this article reveals that unity power factor can only minimize the reactive current, and hence, the conduction loss on the primary bridge but not necessarily give rise to maximum end-to-end power transfer efficiency in this network. This finding leads to another design criterion for the compensation capacitance given that the properties of the load-independent output voltage and current are able to be offered by different values of the parallel compensation capacitance.

The rest of this article is organized as follows. In the light of the similarities of the circuit structures and electrical characteristics, Section II compares the characteristics of the conventional S/S and the proposed dynamic S/SP compensation networks as a CC–CV battery charger. In Section III, the theoretical efficiencies of the dynamic compensation in CC and CV modes are analyzed. In Section IV, the effectiveness of the proposal will be verified by experimental prototype. Finally, the conclusion will be given in Section V.

II. Comparison of S/S and Dynamic S/SP Compensation Networks Under Different Coupling Conditions

Since the characteristics of the S/SP compensation network possess some similarities with the typical S/S compensation network, this section will compare their output voltage and current characteristics and the input impedance angles under the variation of coupling coefficient, hence, the advantages of the dynamic S/SP compensation as a battery charger can be highlighted. Fig. 1 shows the schematic diagram of the IPT converter with dynamic S/SP compensation network for which the series capacitors C_1 and C_2 are intentionally designed to resonate with the leakage inductance L_1 and L_2 while the parallel capacitor C_3, which is electronically variable by SCC, is designed to resonate with the magnetizing inductance $L_{\rm m}$. In addition, the S/SP compensation network is reduced to the conventional S/S compensation network if the value of C_3 tends to be zero. Fig. 2 shows the simplified circuit diagram of the proposed network in a transformer T-model, where all the circuit elements are reflected to the primary side for mathematical analysis. The variables Z_1, Z_2, and Z_3 are introduced in Fig. 2 and expressed in (1) to represent the lumped impedances of C_1 and L_1, C_2 and L_2, and C_3 and $R_{\rm E}$, respectively. The input impedance of the network is given in (2). In a typical design of compensation networks, the input impedance angle is often designed to be slightly inductive rather than purely resistive to facilitate the ZVS operation of the primary bridge without causing significant conduction loss due to the excessive reactive power. Fig. 3 illustrates the theoretical operating waveforms on the primary bridge in which the amplitude of the fundamental component of the bridge voltage $v_{\rm inv}$ is modulated by the duty cycle D and the bridge current $i_{\rm p}$ lags the fundamental component of the bridge voltage (i.e., $v_{\rm inv-1}$) by $\theta_{\rm in}$, which is inductive (i.e., $\theta_{\rm in} > 0$) and the necessary condition for ZVS. Additionally, in order to achieve ZVS operation in all switches, φ should be always greater than zero. Thus, under these conditions, the negative resonant tank current will force to fully discharge the junction capacitance of the MOSFET within sufficient dead time and subsequently flow into the antiparallel diode of the MOSFET, which clamps the drain-to-source voltage of the MOSFET to nearly zero [33]. However, the condition for positive φ could be violated when D is varied and becomes smaller for a given value of $\theta_{\rm in}$ for output voltage/current regulation, as shown in Fig. 3 and expressed mathematically in (3). Therefore, by exploiting the load-independent output characteristics of a compensation network, it can greatly ease the difficulty in rendering ZVS operation of the primary bridge by maximizing D close to unity and restricting its variation over the entire ranges of load and coupling

$$Z_1 = \frac{1}{j\omega C_1} + j\omega L_1 + R_{\rm p} = j\left(\omega L_1 - \frac{1}{\omega C_1}\right) + R_{\rm p}$$

$$Z_2 = \frac{1}{j\omega n^2 C_2} + \frac{j\omega L_2}{n^2} + R_{\rm s} = \frac{j}{n^2}\left(\omega L_2 - \frac{1}{\omega C_2}\right) + R_{\rm s}$$

$$Z_3 = \frac{1}{j\omega n^2 C_3}\frac{R_{\rm E}}{n^2} = \frac{\frac{R_{\rm E}}{n^2}}{1 + j\omega R_{\rm E} C_3}$$

$$Z_{\rm m} = j\omega L_{\rm m} + R_{\rm m} \tag{1}$$

$$Z_{\rm in} = Z_1 + Z_{\rm m}\,(Z_2 + Z_3)$$

$$= Z_1 + \frac{Z_{\rm m}\,(Z_2 + Z_3)}{Z_2 + Z_3 + Z_{\rm m}} \tag{2}$$

$$\varphi = \theta_{\rm in} - \frac{(1-D)\pi}{2} > 0. \tag{3}$$

II. A. Assumptions

The following assumptions are made in the analysis of this section.

(1) The winding and core resistances (i.e., $R_{\rm p}$, $R_{\rm s}$, and $R_{\rm m}$) are neglected.
(2) The ON-resistances of MOSFETS are zero.
(3) The forward voltages of diodes are zero.
(4) The parasitic winding capacitances are neglected.
(5) Fundamental harmonic approximation (FHA) is used.

II. B. Load-Independent Output Voltage

The load-independent output voltage characteristic of S/S and S/SP compensation networks can be readily appreciated by inspecting Fig. 2. From Fig. 2, it can be seen that the output voltage of the networks equal to $v_{\rm inv}$ when Z_1 and Z_2 are nullified by C_1 and C_2 at an identical angular frequency, which is independent of the value of C_3 and expressed by $\omega_{\rm cv}$ in (4). In other words, as compared to the S/S compensation, the presence of C_3 is redundant for obtaining load-independent output voltage but providing additional flexibility for manipulating the input impedance of the network for better power transfer efficiency in CV stage while maintaining load-independent output current in CC stage under varying coupling condition, which will be discussed further in the following sections. The expression of output-voltage-to-input-voltage gain of Fig. 2 is derived and given in (5), where C_3 is zero for the case of S/S compensation

$$\omega_{\rm cv} = \frac{1}{\sqrt{L_1 C_1}} = \frac{1}{\sqrt{L_2 C_2}} \tag{4}$$

$$\frac{v_{\rm o}}{v_{\rm inv}} = \frac{Z_3}{Z_2 + Z_3} \times \frac{Z_{\rm m}\,(Z_2 + Z_3)}{Z_1 + (Z_{\rm m}\,(Z_2 + Z_3))}. \tag{5}$$

When misalignment or air gap variation occurs, the leakage and magnetizing inductances will change accordingly and can be reflected by coupling coefficient k. As a result, the characteristic of load-independent output voltage of both networks is lost. Even though the input impedances of both networks are still inductive (i.e., $\theta_{\rm in} > 0$) when the coils are misaligned or the air gap is increased, other control methods instead of pulsewidth modulation for output voltage regulation are still highly desirable as the duty cycle of the primary bridge voltage can be maximized for the ease of the realization of ZVS on the primary bridge [29]. As revealed in [29] and shown in (6), the ratio of the primary and secondary leakage inductances is approximately constant and related to the turns ratio only. Therefore, the method of switching frequency modulation works satisfactorily for output voltage regulation by tracking the change of $\omega_{\rm cv}$, and hence, the leakage inductances can be well compensated in both S/S and S/SP compensation networks under the variation of coupling [29]. Nevertheless, as benefited from the controllability of C_3 in the dynamic S/SP compensation network, the input reactive power, and hence, the power transfer efficiency of the dynamic S/SP compensation network can always be adjusted in the CV stage under different coupling conditions

$$n \approx \sqrt{\frac{L_{\rm s}}{L_{\rm p}}}$$

$$k = \frac{nL_{\rm m}}{\sqrt{L_{\rm p} L_{\rm s}}} \tag{6}$$

$$L_{\rm p} = L_1 + L_{\rm m}$$

$$L_{\rm s} = L_2 + n^2 L_{\rm m}$$

$$\frac{L_2}{L_1} \approx n^2. \tag{7}$$

II. C. Load-Independent Output Current

The characteristic of load-independent output current in S/S compensation is widely discussed while it is also explored recently in a few literature in S/SP compensation [21], [34]. By transforming Fig. 2 into π-network, the equivalent representation of load-independent output current of the dynamic S/SP compensation is graphically shown in Fig. 4 given that all the parallel impedance branches are in resonance and effectively open-circuit at certain frequency, where $Z_{\rm A}$, $Z_{\rm B}$, and $Z_{\rm C}$ are expressed in (8). Intuitively, it is feasible to design the magnitude of the load-independent output current by $Z_{\rm B}$ via switching frequency and matching the value of C_3 to the designed frequency such that C_3 is resonating with $Z_{\rm B}$ and $Z_{\rm C}$ in Fig. 4. Here, a general mathematical expression of output-current-to-input-voltage gain for both networks is derived from (5) and given in (9). By equating λ in the denominator of (9) to zero, the condition for achieving load-independent output current in S/S and S/SP compensations can be found. Similar to the last section, by substituting $C_3 = 0$ into λ, the condition for S/S compensation for achieving load-independent output current is solved, which is given in (10)

$$Z_{\rm A} = \frac{Z_1 Z_2 + Z_{\rm m}\,(Z_1 + Z_2)}{Z_2}$$

$$Z_{\rm B} = \frac{Z_1 Z_2 + Z_{\rm m}\,(Z_1 + Z_2)}{Z_{\rm m}}$$

$$Z_{\rm C} = \frac{Z_1 Z_2 + Z_{\rm m}\,(Z_1 + Z_2)}{Z_1} \tag{8}$$

$$\frac{i_{\rm o}}{v_{\rm inv}} = \frac{j\omega L_{\rm m}}{Z_1 Z_2 + j\omega L_{\rm m}\,(Z_1 + Z_2) + \lambda R_{\rm E}} \tag{9}$$

where $\lambda = j\omega L_{\rm m} + Z_1 + j\omega n^2 C_3 Z_1 Z_2 - \omega^2 L_{\rm m} n^2 C_3 (Z_1 + Z_2)$.

However, as can be seen from (10) and (11), the frequency and the magnitude of the load-independent output current of S/S

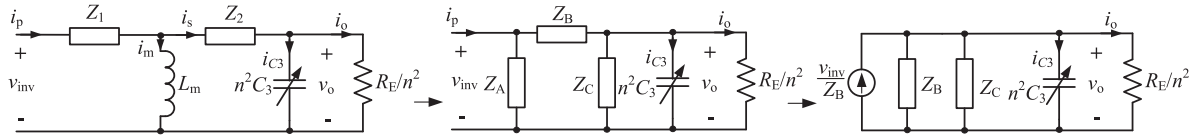

Fig. 4. Transformation of the dynamic S/SP compensation network into the equivalent circuit of load-independent current output.

compensation are automatically fixed with no design freedom once the magnetizing inductance is determined by the coupling condition and the values of C_1 and C_2 are predetermined by (4) for the set-point of load-independent output voltage under the nominal coupling condition as explained in the last section. As a result, the operating frequency for load-independent output current and the magnitude of the charging current is inflexible to be designed for various rates of charging process. It should be noted that the input impedance angle for S/S compensation in load-independent output current mode is resistive due to the cancellation of self-inductances by C_1 and C_2 at $\omega_{\mathrm{cc(S/S)}}$, which is well explained in the literature. The unity power factor and the modulation of primary bridge voltage for desirable magnitude of output current make the realization of ZVS more challenging.

On the contrary, for the case of S/SP compensation, C_3 is a nonzero value. By further expanding the expression of λ, another equation is obtained, which can be used to solve for the relationship between C_3 and the switching frequency for different magnitudes of load-independent output current, as shown in (12). Since (12) is a fourth-order equation, the solution of (12) has four roots and only the positive real roots are considered for a particular value of C_3. Compared with S/S compensation, it can be found that the switching frequency for achieving load-independent output current in S/SP compensation is not unique but can be determined in conjunction with the value of C_3. Therefore, the magnitude and the operating frequency of the load-independent output current could be designed in contrast to the S/S compensation, which is desirable for the applications requiring for various rates of charging without modulating the primary bridge voltage

$$\omega_{\mathrm{cc(S/S)}} = \frac{1}{\sqrt{(L_1 + L_{\mathrm{m}})\, C_1}} = \frac{1}{\sqrt{L_{\mathrm{p}} C_1}} \tag{10}$$

$$\left| \frac{i_{\mathrm{o}}}{v_{\mathrm{inv}}} \right|_{\omega=\omega_{\mathrm{cc(S/S)}}} = \frac{1}{\omega_{\mathrm{cc}} L_{\mathrm{m}}} \tag{11}$$

$$a\omega^4 - b\omega^2 + c = 0$$

$$\rightarrow \omega_{\mathrm{cc(S/SP)}} = \pm\sqrt{\frac{-b \pm \sqrt{b^2 - 4ac}}{2a}} \tag{12}$$

where

$$a = n^2 C_3 \left(L_{\mathrm{m}} L_1 + \frac{L_{\mathrm{m}} L_2}{n^2} + \frac{L_1 L_2}{n^2} \right)$$

$$b = n^2 C_3 L_{\mathrm{m}} \left(\frac{1}{C_1} + \frac{1}{n^2 C_2} \right) + C_3 \left(\frac{L_2}{C_1} + \frac{L_1}{C_2} \right) + L_{\mathrm{m}} + L_1$$

$$c = \frac{C_3}{C_1 C_2} + \frac{1}{C_1}. \tag{13}$$

Again, the effects of coupling variation to the characteristics of load-independent output current and input impedance angle are studied here. For S/S compensation, as mentioned earlier and shown in (10), the switching frequency for load-independent output current is only dependent on L_{p} and C_1. Nevertheless, L_{p} and L_{s} are relatively constant as the coupling coefficient is changed. In other words, the operating frequency and the input impedance angle of S/S compensation network are almost fixed while the output current is sensitive to the coupling condition and inversely proportional to the magnetizing inductance as expressed in (11), which implies wide range of pulse-width modulation of the primary bridge voltage for output current regulation, possibly leading to the violation of ZVS condition. On the other hand, for dynamic S/SP compensation, the extra freedom offered by C_3 can be used to restore the characteristics at the designed coupling condition by modulating the value of C_3 in conjunction with the switching frequency.

III. Efficiency Analysis and Control of Dynamic S/SP Compensation Network With SCC

As analyzed in the last section, the controllability of C_3 in the dynamic S/SP compensation network can provide a better performance in achieving and maintaining load-independent outputs as compared with the conventional S/S compensation under different coupling conditions. For the load-independent output current in the CC stage, the magnitude of the charging current can be flexibly fixed by modulating the value of C_3 and switching frequency simultaneously. When the charging stage is switched to the CV stage, the load-independent output voltage can be maintained by switching frequency modulation while the redundancy of C_3 can be used to optimize the input reactive power for higher power transfer efficiency. Nevertheless, since the addition of C_3 inevitably introduces extra conduction loss, this section is of interest to analyze the design criterion for C_3 given that different values of C_3 can give rise to the properties of load-independent output voltage and current simultaneously.

III. A. Efficiency Analysis of Dynamic S/SP Compensation Network in CV and CC Modes

Table I tabulates the transformer parameters used in the following sections, which is a typical circular pad with its physical dimensions listed in [29]. The inductances of the loosely coupled transformer are measured under different air gap and misalignment conditions. The turns ratio of the transformer n is about 1.083. The values of C_1 and C_2 are determined based on the nominal coupling condition (i.e., k_1) at the specified switching frequency (i.e., 85 kHz). Given that the measured value of R_{p}, R_{s}, and R_{m} are 0.487, 0.454, and $0.534\,\Omega$, respectively, the theoretical efficiency of the network in the load-independent

TABLE I
MEASURED PARAMETERS OF LOOSELY COUPLED TRANSFORMER

Condition	air gap (cm)	misalignment (cm)	k	$L_1(\mu\text{H})$	$L_2(\mu\text{H})$	$L_\text{m}(\mu\text{H})$	L_2/L_1
k_1 (nominal)	10	0	0.4144	381.72	414.68	246.63	1.086
k_2	10	16	0.2553	457.98	502.15	147.94	1.096
k_3	16	0	0.2474	454.57	503.58	141.74	1.107
k_4	16	16	0.1617	498.06	546.92	91.62	1.098

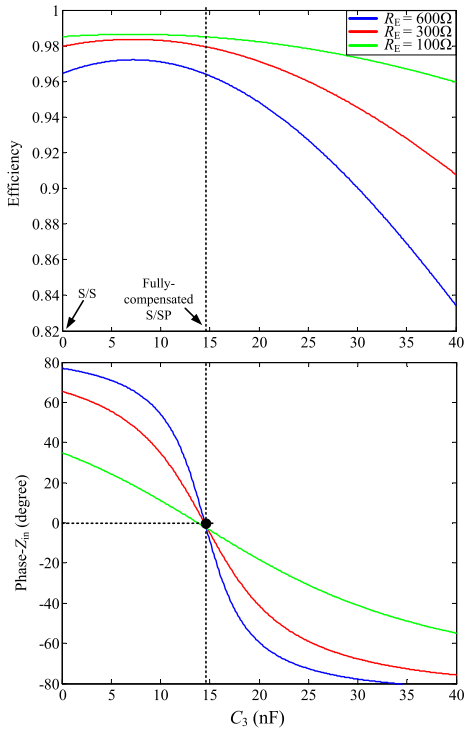

Fig. 5. Theoretical efficiencies and the input phase angles of the dynamic S/SP compensation network versus the value of C_3 in load-independent voltage mode under k_1 condition.

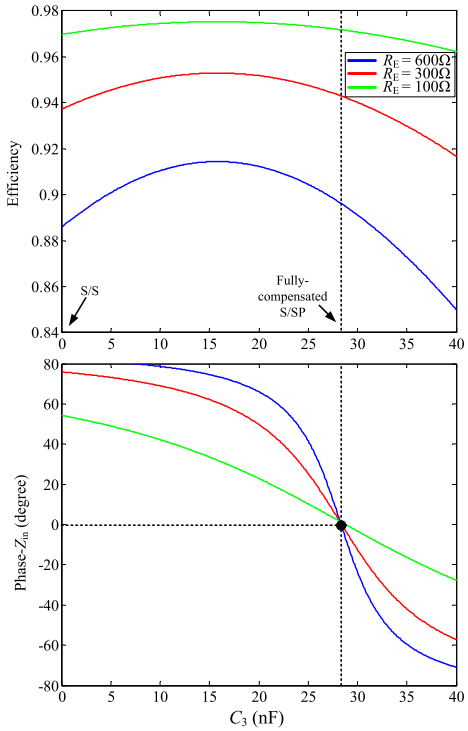

Fig. 6. Theoretical efficiencies and the input phase angles of the dynamic S/SP compensation network versus the value of C_3 in load-independent voltage mode under k_3 condition.

voltage mode can be calculated by substituting (2), (4), and (5) into (14). Figs. 5 and 6 plot the theoretical efficiencies and the input impedance angles of the dynamic S/SP compensation network versus the value of C_3 under the conditions of k_1 and k_3, respectively. From these figures, it can be seen that the efficiency curves with different R_E are parabolic and peak at the same value of C_3 under the same coupling condition, where L_m is partially compensated. Moreover, the phenomenon becomes more prominent under weak coupling condition (i.e., k_3), as shown in Fig. 6. In other words, the operating point of C_3 for maximum efficiency is located between the cases of S/S and fully compensated S/SP compensation networks. The physical significance of the parabolic shape of the efficiency curves can be explained by the power loss of the network, which neglects the switching loss of the primary bridge and considers only the conduction losses due to the presence of R_p, R_s, and R_m, respectively, as expressed in (15). As shown by (15), the power loss originated from i_p and R_p monotonically decreases with increasing C_3, and vice versa for i_s and R_s. Therefore, the power loss is initially dominated by i_p when C_3 is increased from zero and gradually dominated by i_s as C_3 is kept increasing until which L_m is fully compensated while i_p attains its minimum. By differentiating (15) with respect to C_3 and equating the derivative to zero, the value of C_3 for maximum efficiency point can be found as shown in (16), which is irrelevant to the load resistance. Therefore, the efficiency of the network can always be maximized in the CV stage of a charging process by adjusting the effective value of C_3 by SCC

$$\begin{aligned} P_\text{i} &= \text{Re}\left[\frac{v_{\text{inv(rms)}}^2}{Z_\text{in}^*}\right] = \frac{v_{\text{inv(rms)}}^2}{|Z_\text{in}|}\cos\theta_\text{in} \\ P_\text{o} &= \text{Re}\left[\frac{v_{\text{o(rms)}}^2}{R_\text{E}}\right] = \frac{v_{\text{inv(rms)}}^2\left|\frac{v_\text{o}}{v_\text{inv}}\right|^2}{R_\text{E}} \\ \eta &= \frac{P_\text{o}}{P_\text{i}} \end{aligned} \tag{14}$$

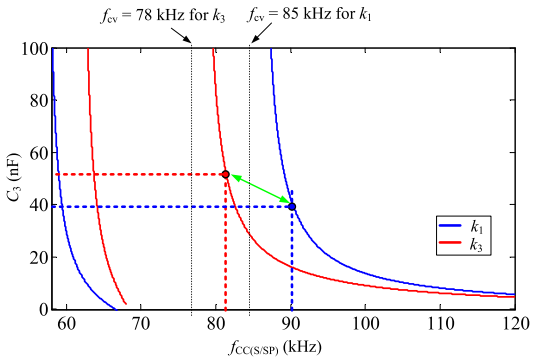

Fig. 7. Relationship between the value of C_3 and switching frequency for obtaining load-independent output current under k_1 and k_3 conditions.

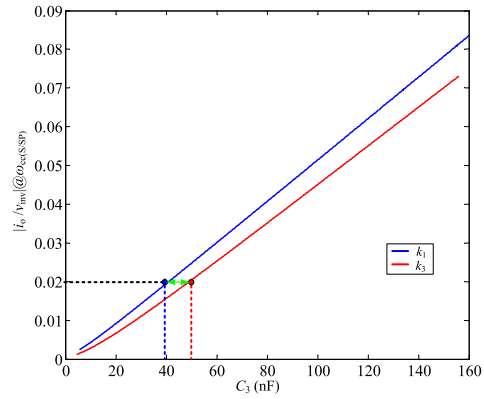

Fig. 8. Relationship between the magnitude of load-independent output-current-to-input-voltage gains and the value of C_3 under k_1 and k_3 conditions.

$$P_{\text{loss(cv)}} = i_{\text{p}}^2 R_{\text{p}} + i_{\text{s}}^2 R_{\text{s}} + i_{\text{m}}^2 R_{\text{m}} = \left(\sqrt{(\omega_{\text{cv}} v_{\text{o}} C_3 - i_{\text{m}})^2 + i_{\text{o}}^2}\right)^2 R_{\text{p}} + \left(\sqrt{(\omega_{\text{cv}} v_{\text{o}} C_3)^2 + i_{\text{o}}^2}\right)^2 R_{\text{s}} + i_{\text{m}}^2 R_{\text{m}} \tag{15}$$

$$\frac{\mathrm{d}P_{\text{loss(cv)}}}{\mathrm{d}C_3} = 0 \rightarrow C_{3(\text{op})} = \frac{1}{\omega_{\text{cv}}^2 L_{\text{m}}} \times \frac{R_{\text{p}}}{R_{\text{p}} + R_{\text{s}}}. \tag{16}$$

Likewise, the efficiency analysis on load-independent current mode of the dynamic S/SP compensation network can also be made by sweeping the value of C_3 and the corresponding ω_{cc} using (12) and substituting them into (14). Fig. 7 plots the combinations of C_3 and switching frequency for obtaining load-independent output current in S/SP compensation using (12) under k_1 and k_3 conditions. From Fig. 7, it is interesting to observe that the solution is discontinuous and tends to infinity when the frequency approaches 85 and 58 kHz and 78 and 62 kHz, respectively, under k_1 and k_3 conditions. In fact, these frequencies correspond exactly to the points that load-independent output voltage is achieved under k_1 and k_3 conditions. Therefore, it is reasonable to observe that no solutions for load-independent output current are coexisting when the frequency is approaching to the point where load-independent output voltage is achieved. Here, only the solutions larger than ω_{cv} are considered due to its wider available range. As analyzed in the last section and seen in Fig. 8, the magnitude of the output-current-to-input-voltage gain of the network varies with the value of C_3. Even though the output current of the network is adjustable and can be made higher by increasing the value of C_3, it is important to study the resulting input impedance angle and the power conversion efficiency of the network such that the input reactive power and the associated power losses are acceptable. Figs. 9 and 10 plot the theoretical efficiencies and the input impedance angles of the dynamic S/SP compensation network versus the value of C_3 under k_1 and k_3 conditions for load-independent output current. As can be seen from the figures, the input impedance angle of the network is inductive and the input current of the network tends to be in-phase with the inverter voltage as the value of C_3 is increased. However, it does not imply that the power transfer efficiency monotonically increases with the value of C_3 as the input reactive power reduces. Instead, similar to the case of load-independent output voltage, the efficiency curves for load-independent output current attain their maximum values in the inductive input impedance region and degrade more rapidly when the values of C_3 and R_{E} are higher. The efficiency droop can be simply explained by the transformer T-model in

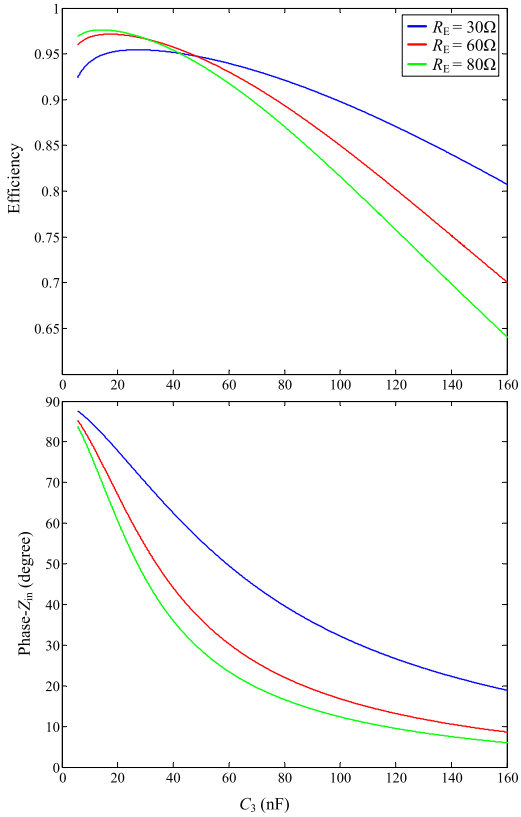

Fig. 9. Theoretical efficiencies and the input phase angles of the dynamic S/SP compensation network versus the value of C_3 in load-independent current mode under k_1 condition.

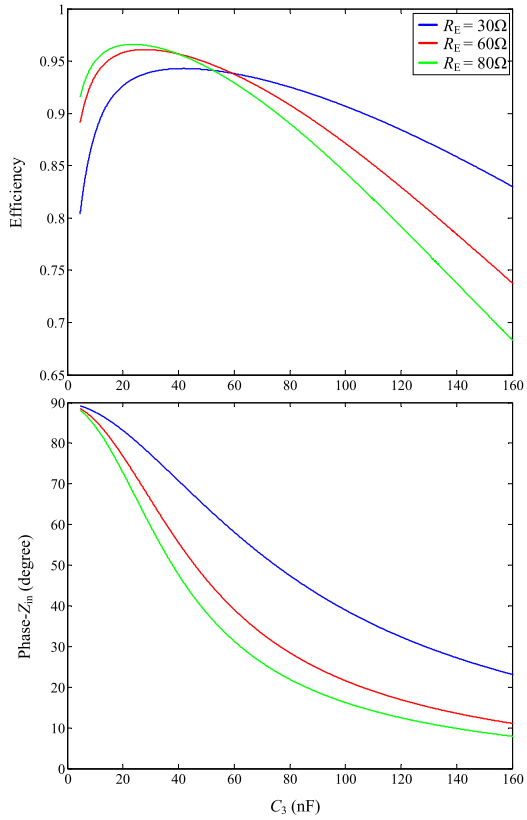

Fig. 10. Theoretical efficiencies and the input phase angles of the dynamic S/SP compensation network versus the value of C_3 in load-independent current mode under k_3 condition.

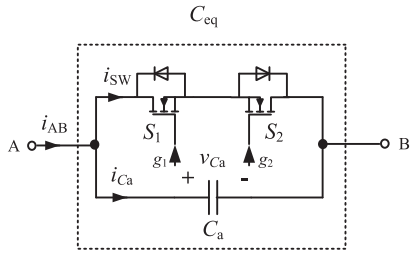

Fig. 11. Schematic diagram of SCC.

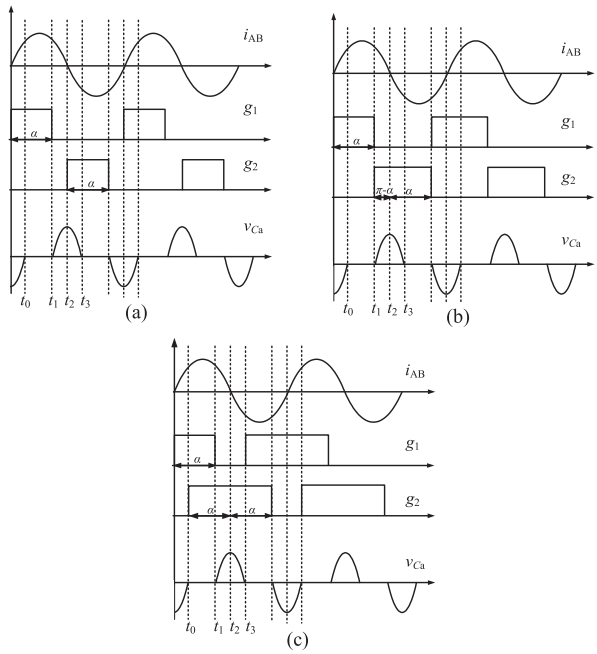

Fig. 12. Key waveforms of SCC with different modulation methods.

Fig. 4. When i_o is increased by C_3 as the relationship plotted in Fig. 8, more current is naturally drawn from the input due to the increased output power. However, the lower impedance path created by the increased C_3 tends to prevent the current from delivering to the output and demands more current from the input (i.e., $\uparrow \overrightarrow{i_o} = \uparrow (\overrightarrow{i_p} - \overrightarrow{i_m}) - \uparrow \overrightarrow{i_{C3}}$), leading to dramatic increases in circulating current and transformer losses even if the input impedance tends to be resistive as C_3 increases. In other words, the higher control degree of freedom of the dynamic S/SP compensation network in the load-independent current mode is gained at the expense of lower efficiency, which is generally lower than the S/S compensation network. As a result, the ranges of C_3 and the charging current in the CC stage should be bounded near the peak of the efficiency curves if minimum power transfer efficiency is specified as one of the design requirements as outlined in [35].

III. B. Control of the Dynamic S/SP Compensation Network to Achieving CV and CC Outputs With SCC

After the efficiency analysis of the dynamic S/SP compensation network, the working principle of SCC for modulating the effective value of C_3 is briefly explained here to facilitate the discussion on its control in the rest of the section. Fig. 11 shows the schematic diagram of an SCC, which consists of a fixed capacitor C_a and two back-to-back active switches. By controlling the phase-shifts of the gate signals of the switches relative to the terminal current i_{AB}, the current flowing through C_a can be controlled, and hence, the effective resonant capacitance C_{eq} can be varied by the fundamental component of v_{Ca}, as shown in Fig. 12. To achieve the same goal, different modulation methods of SCC have been proposed in which the basic principle of SCC does not alter significantly but specifically the conduction loss can be reduced by the improved modulation in Fig. 12(c) due to the conduction of the MOSFETs instead of the body diodes as reported in [36]. The operation of SCC is already well discussed in previous papers and will not be repeated here for simplicity [36].

From the operation principle of SCC, it is found that ZVS can be intrinsically realized in all methods such that the resulting converter efficiency will not degrade significantly. By decomposing the waveform of v_{Ca} into harmonic component using Fourier series and considering only the fundamental component, the amplitude of v_{Ca} can be expressed by (17) and the equivalent capacitance can be derived and is given by (18) in terms of

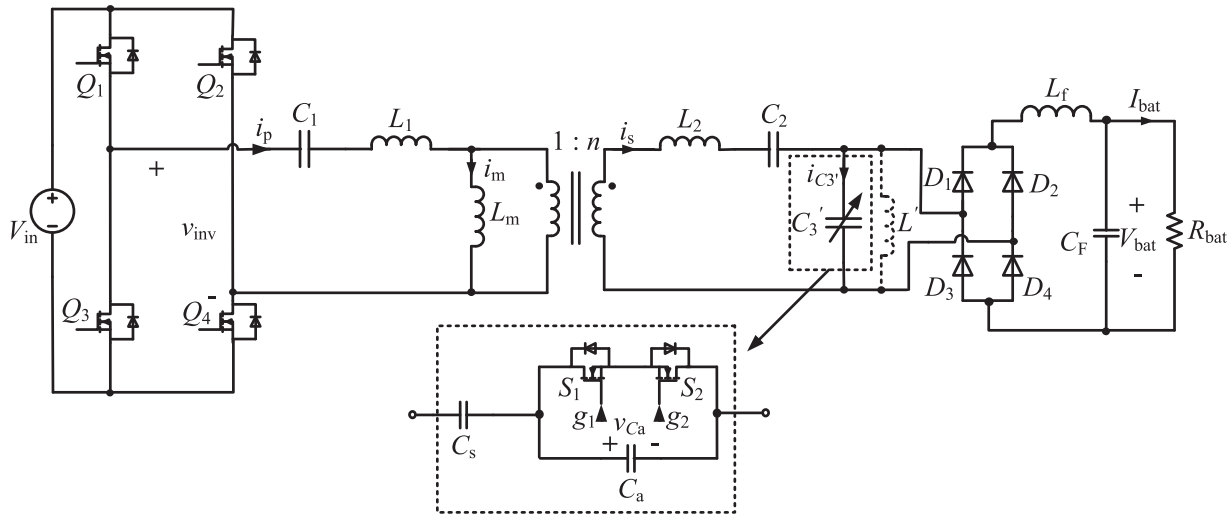

Fig. 13. Completed schematic diagram of the proposed dynamic S/SP compensated IPT converter with SCC.

α [37]. As analyzed previously, the switching frequency and the effective value of C_3 (i.e., α) in the CC and CV stages depend on the transformer parameters. In stationary applications in practice, the computation and control complexity can be simplified if the displacement of the secondary coil is divided into several zones and the corresponding values of switching frequency and α are preloaded into the controller [38]. Hence, the controller can select the values of switching frequency and α from the look-up table given that the relative position of the secondary coil is known via the communication between the primary and secondary before the start of a charging process or the transition of CC to CV stage

$$v_{Ca} = \frac{i_{AB}}{\omega C_a}\left[2 - \frac{1}{\pi}\left(2\alpha - \sin 2\alpha\right)\right] \tag{17}$$

$$v_{Ca} = \frac{i_{AB}}{\omega C_{eq}} \Rightarrow C_{eq}(\alpha) = \frac{C_a}{2 - \left(2\alpha - \sin 2\alpha\right)/\pi} \tag{18}$$

where $90^\circ \leqslant \alpha < 180^\circ$

IV. Experimental Verification

The prototype of the IPT converter with the proposed dynamic S/SP compensation network for delivering CC and CV outputs was constructed for experimental verification. Fig. 13 shows the completed schematic diagram of the prototype. The design procedure of the IPT converter is systematically presented as follows and the finalized component values are tabulated in Table II. The Li-ion battery is emulated by an electronic load varying from 25 to 135 Ω. The prototype was tested under the conditions of k_1 and k_3, where the transformer parameters are listed in Table I for demonstrating the effectiveness of the proposal under varying coupling condition.

Step 1: Specify the ranges of air gap and misalignment and measure the leakage and magnetizing inductances under the extreme coupling conditions.

Step 2: Specify the switching frequency for load-independent output voltage and calculate the value of C_1 and C_2 under the nominal coupling condition (i.e., maximum coupling coefficient) using (4). In this article, the switching frequency is chosen as 85 kHz for k_1 condition. Calculate the switching frequency under the minimum coupling condition using (4), which defines the minimum switching frequency of the converter, which is about 78 kHz for k_3 condition.

Step 3: Specify the minimum efficiency and find the achievable range of load-independent output-current-to-input-voltage gain under the extreme coupling conditions, which can be graphically solved by Figs. 8–10. Here, the load-independent output-current-to-input-voltage gain is fixed to be 0.02 A/V throughout the experimental verification so that the theoretical efficiency is well-above as 90%. The switching frequency for load-independent current mode under the maximum coupling condition defines the maximum switching frequency of the

TABLE II
Hardware Specifications

Parameter	Value
V_{in}	200 V
V_{bat}	145 V
I_{bat}	4 A
C_1	8.972 nF
C_2	8.271 nF
C_s	60 nF
C_a	10 nF
C_F	6.6 μF
L_f	1 mH
L'	100 μH
R_{bat}	25 Ω – 135 Ω
Digital controller	Texas TMS320F28335
$Q_1 - Q_4$, $D_1 - D_4$, $S_1 - S_2$	UJC06505K
Output power	150 W – 880 W

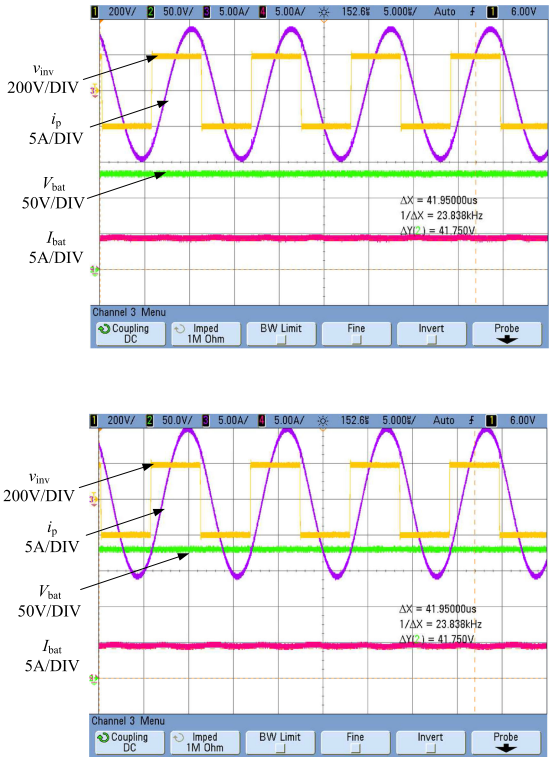

Fig. 14. Experimental waveforms of $v_{\rm inv}$, $i_{\rm p}$, $V_{\rm bat}$, and $I_{\rm bat}$ for load-independent current mode under k_1 condition with $R_{\rm bat} = 25\,\Omega$ and $R_{\rm bat} = 40\,\Omega$, respectively. (upper) $R_{\rm bat} = 25\,\Omega$, and (lower) $R_{\rm bat} = 40\,\Omega$.

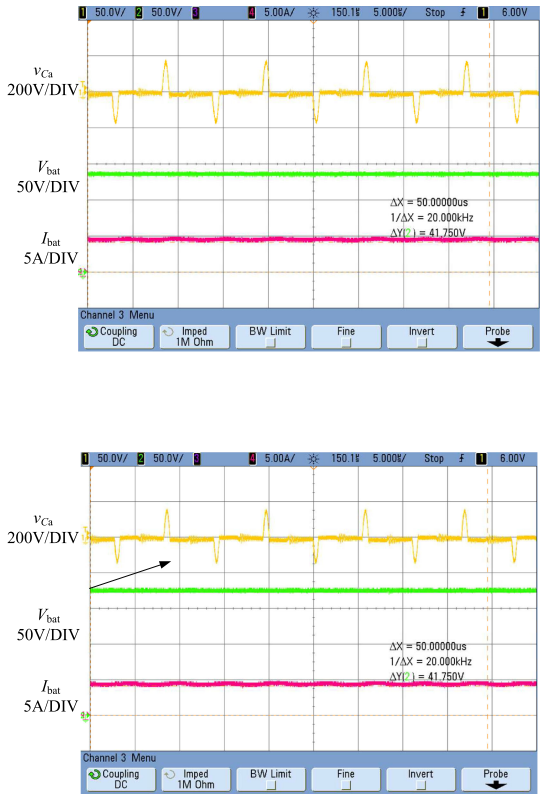

Fig. 15. Experimental waveforms of v_{Ca}, $V_{\rm bat}$, and $I_{\rm bat}$ for load-independent current mode under k_1 condition with $R_{\rm bat} = 25\,\Omega$ and $R_{\rm bat} = 40\,\Omega$, respectively. (upper) $R_{\rm bat} = 25\,\Omega$, and (lower) $R_{\rm bat} = 40\,\Omega$.

converter. Therefore, the frequency variation of the converter is limited between $\omega_{\rm cv@}{}_{k_3} \leqslant \omega \leqslant \omega_{\rm cc@}{}_{k_1}$.

Step 4: Calculate the required values of $C_{\rm s}$ and $C_{\rm a}$ such that the effective value of C_3 can be modulated continuously between the values of $C_{\rm s}//C_{\rm a}$ and $C_{\rm s}$ to cover the required range of C_3.

Step 5: Simulation should be performed to verify the design. Since the theoretical analysis is based on the FHA, the nonlinearity of the output diode rectification may lead to discontinuous conduction mode of output voltage if the battery equivalent resistance is beyond the load boundary [39]. An additional inductor L' is optional to be connected in parallel with C_3 to extend the load range for continuous conduction mode [39]. In this case, the equivalent impedance of the paralleled L' and C_3' should satisfy (19) and the values of $C_{\rm s}$ and $C_{\rm a}$ should be recalculated for $C_3{}'$. The value of $C_3{}'$ is given by (20) in terms of $C_{\rm s}$, $C_{\rm a}$, and α

$$\frac{1}{j\omega C_3} = \frac{1}{j\omega C_3{}'} // j\omega L' \tag{19}$$

$$C_3{}'(\alpha) = \frac{\pi C_{\rm s} C_{\rm a}}{\pi C_{\rm a} + C_{\rm s}\left(2\pi - 2\alpha + \sin 2\alpha\right)}. \tag{20}$$

Fig. 14 shows the experimental waveforms of the load-independent current mode of the converter with different battery equivalent resistances (i.e., $R_{\rm bat} = 25\,\Omega$ and $R_{\rm bat} = 40\,\Omega$) under k_1 condition. The required equivalent value of C_3 is about 40 nF and the switching frequency is 90 kHz. As can be seen from the figure, the input impedance is inductive as predicted in the previous section and the battery charging current in the CC stage can be kept almost constant even no modulation is performed on the primary bridge, which are favorable for the realization of ZVS. Fig. 15 shows the corresponding experimental waveform of SCC in the load-independent current mode for which α is equal to 165° for $R_{\rm bat} = 25\,\Omega$ and $R_{\rm bat} = 40\,\Omega$, respectively.

Figs. 16 and 17 show the experimental waveforms of the load-independent voltage mode of the converter for heavy load (i.e., $R_{\rm bat} = 40\,\Omega$) and light load (i.e., $R_{\rm bat} = 135\,\Omega$), respectively, with different α under k_1 condition. The switching frequency of this mode under k_1 condition is about 85 kHz. As can be seen, even if the effective value of C_3 is changed by α as noticed by the phase-shift and/or the magnitude of $i_{\rm p}$, the property of load-independent output voltage and its magnitude are still maintained while higher efficiency can be achieved for smaller C_3 (i.e., $\alpha = 120°$), at which more reactive power is drawn from the input. More experimental results on the power transfer efficiency will be provided in Figs. 27 and 28. Fig. 18 shows the corresponding SCC waveforms for $R_{\rm bat} = 135\,\Omega$ with different α while Fig. 19 shows the blown-up waveforms of v_{Ca} and $v_{\rm g1}$.

Fig. 20 shows the experimental waveforms of the load-independent current mode of the converter with different battery equivalent resistances under k_3 condition. Under this condition, the required equivalent value of C_3 and the switching frequency are changed to 50 nF and 82.1 kHz, respectively, in order to

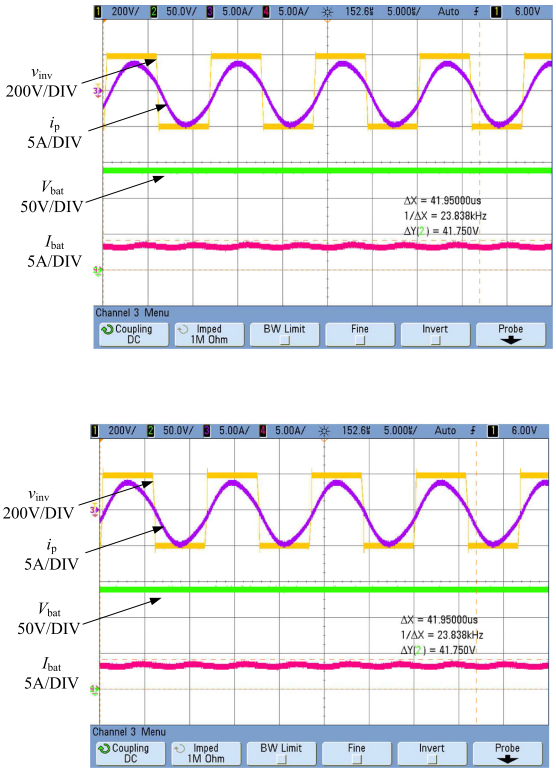

Fig. 16. Experimental waveforms of v_{inv}, i_{p}, V_{bat}, and I_{bat} for load-independent voltage mode for $R_{\mathrm{bat}} = 40\,\Omega$ under k_1 condition with $\alpha = 120^\circ$ and $\alpha = 130^\circ$, respectively. (upper) $\alpha = 120^\circ$, and (lower) $\alpha = 130^\circ$.

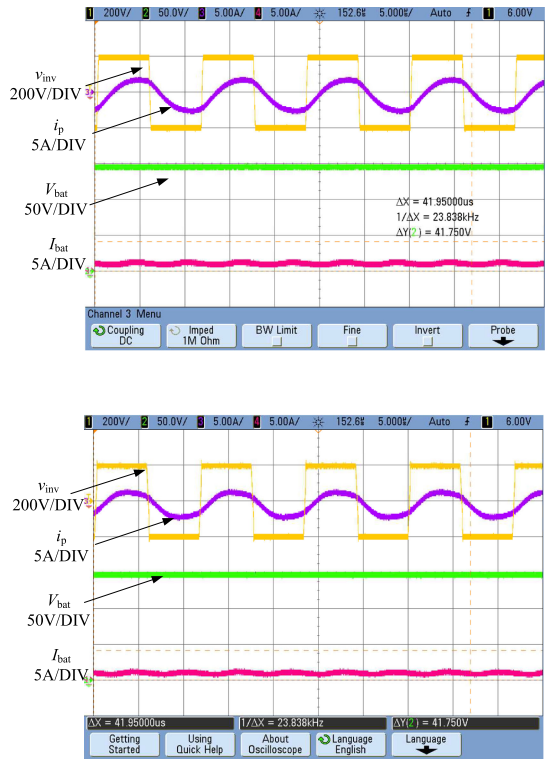

Fig. 17. Experimental waveforms of v_{inv}, i_{p}, V_{bat}, and I_{bat} for load-independent voltage mode for $R_{\mathrm{bat}} = 135\,\Omega$ under k_1 condition with $\alpha = 120^\circ$ and $\alpha = 130^\circ$, respectively. (upper) $\alpha = 120^\circ$, and (lower) $\alpha = 130^\circ$.

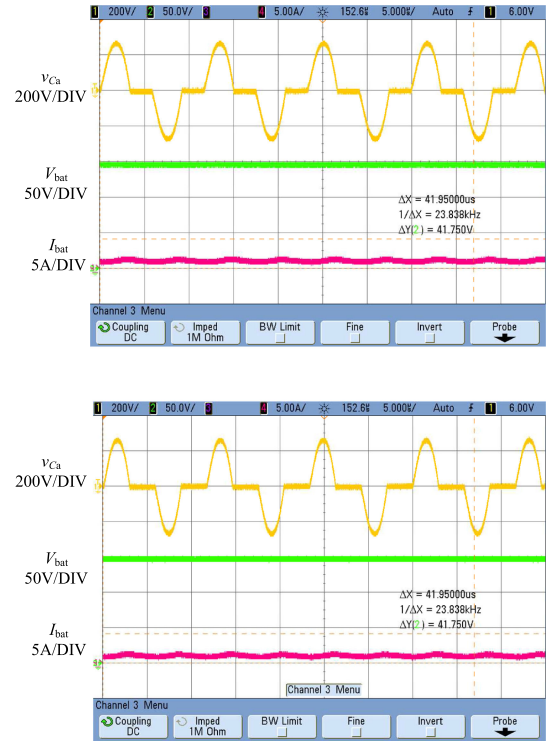

Fig. 18. Experimental waveforms of v_{Ca}, V_{bat}, and I_{bat} for load-independent voltage mode for $R_{\mathrm{bat}} = 135\,\Omega$ under k_1 condition with $\alpha = 120^\circ$ and $\alpha = 130^\circ$, respectively. (upper) $\alpha = 120^\circ$, and (lower) $\alpha = 130^\circ$.

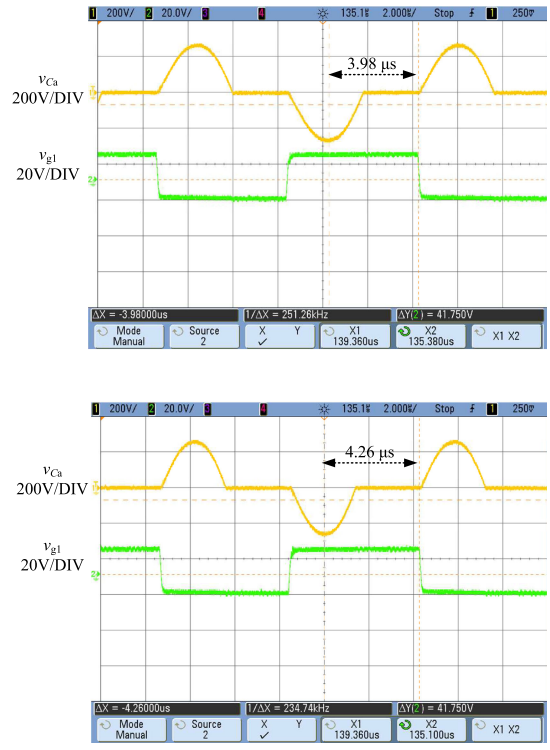

Fig. 19. Experimental waveforms of v_{Ca} and v_{g1} for load-independent voltage mode for $R_{\mathrm{bat}} = 135\,\Omega$ under k_1 condition with $\alpha = 120^\circ$ and $\alpha = 130^\circ$, respectively. (upper) $\alpha = 120^\circ$, and (lower) $\alpha = 130^\circ$.

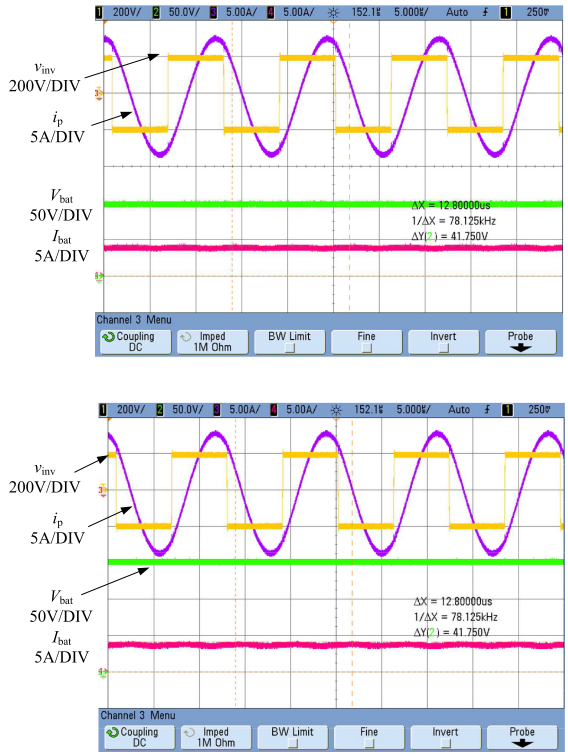

Fig. 20. Experimental waveforms of $v_{\rm inv}$, $i_{\rm p}$, $V_{\rm bat}$, and $I_{\rm bat}$ for load-independent current mode under k_3 condition with $R_{\rm bat} = 25\,\Omega$ and $R_{\rm bat} = 40\,\Omega$, respectively. (upper) $R_{\rm bat} = 25\,\Omega$, and (lower) $R_{\rm bat} = 40\,\Omega$.

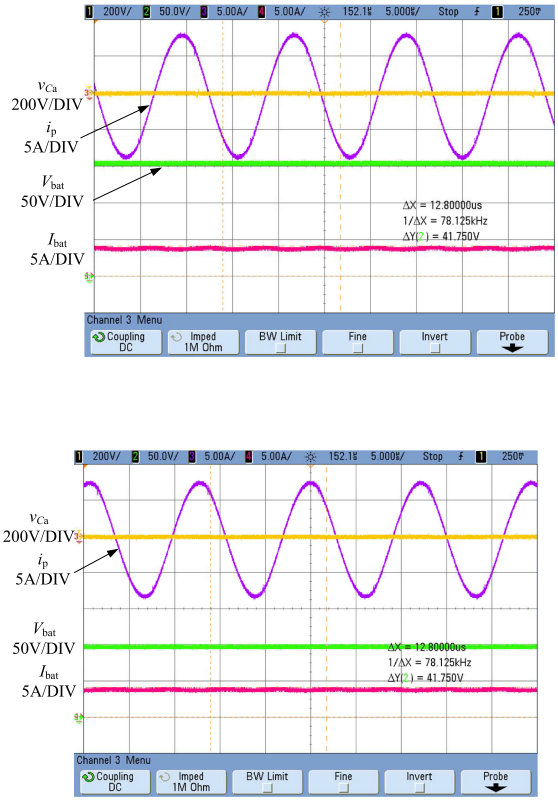

Fig. 21. Experimental waveforms of v_{Ca}, $V_{\rm bat}$, and $I_{\rm bat}$ for load-independent current mode under k_3 condition with $R_{\rm bat} = 25\,\Omega$ and $R_{\rm bat} = 40\,\Omega$, respectively. (upper) $R_{\rm bat} = 25\,\Omega$, and (lower) $R_{\rm bat} = 40\,\Omega$.

recover the magnitude of the load-independent output current as in the k_1 condition to avoid wide range of modulation on the primary bridge for the ease of the realization of ZVS. Fig. 21 shows the associated SCC waveforms from which it can be seen that v_{Ca} is close to zero, which indicates the maximum equivalent value of C_3.

Figs. 22 and 23 show the experimental waveforms of the load-independent voltage mode of the converter for heavy load (i.e., $R_{\rm bat} = 40\,\Omega$) and light load (i.e., $R_{\rm bat} = 135\,\Omega$), respectively, with different α under k_3 condition. The switching frequency for obtaining load-independent output voltage under k_3 condition is about 78 kHz. Similar to k_1 condition and as analyzed in the previous section, the magnitude of the load-independent output voltage is independent of the effective value of C_3. Fig. 24 shows the SCC waveforms of the load-independent voltage mode for $R_{\rm bat} = 135\,\Omega$ with different α under k_3 condition and Fig. 25 shows the blown-up waveforms of v_{Ca} and v_{g1}.

Fig. 26 shows the variations of battery voltage and current in the CC and CV stages without the modulation of the primary bridge. As verified once again, the battery voltage and current can be kept almost constant in their respective stages even under the variation of coupling condition. Without the modulation of the primary bridge, the voltage variations in the CV stage under k_1 and k_3 conditions are 5.58% and 8.06%, respectively. While for the current variations in the CC stage, they are -0.13% and -2.62%, respectively, under k_1 and k_3 conditions. Moreover, the effective value of C_3 in the CV stage does not compromise the magnitude of the load-independent output voltage. Instead, the extra flexibility in the CV stage can be used for the optimization between the power transfer efficiency and input reactive power. Fig. 27 plots the efficiencies of the proposed converter in the CV stage versus the effective value of C_3 under different $R_{\rm bat}$ from which it can be seen that the experimental efficiency trends are in agreement with the analysis of Figs. 5 and 6 in which the curves are parabolic. In the CV stage under k_1 condition, the peak efficiencies of 95.6% and 94.42% can be achieved under heavy and light load conditions by the modulation of SCC. Similarly, in the CV stage under k_3 condition, the peak efficiencies of 94.28% and 91.66% can be achieved under heavy and light load conditions. Fig. 28 plots the overall efficiencies of the converter from CC to CV stage in which different α is applied in the CV stage. The average efficiency in the CC stage under k_1 and k_3 conditions are 88.40% and 88.10%, respectively. While for the average efficiency in the CV stage, they are about 95.09% at $\alpha = 125^\circ$ and 93.41% at $\alpha = 132^\circ$ under k_1 and k_3 conditions, respectively. The differences between the measured and the theoretical efficiencies in the CC and CV stages could be originated from the errors in the measured resistances and other miscellaneous losses in the MOSFETs, diodes, inductors, and the loosely coupled transformer. Finally, a photo of the experimental setup is shown in Fig. 29.

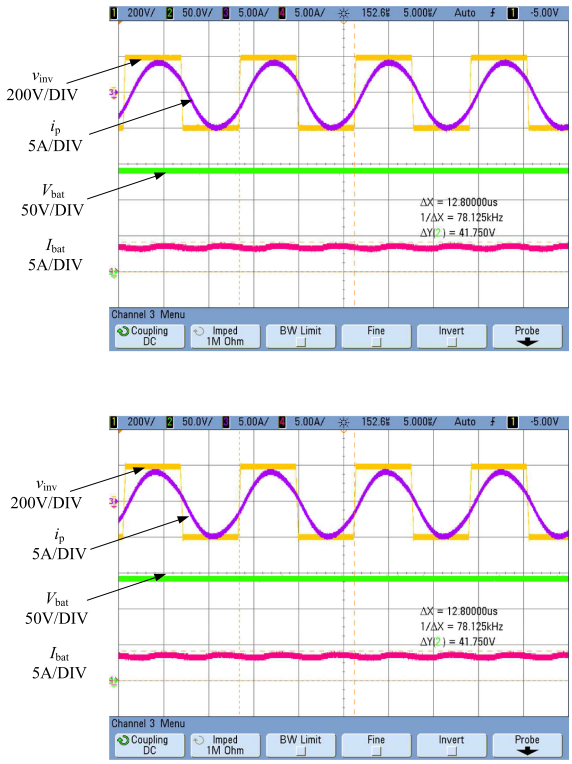

Fig. 22. Experimental waveforms of $v_{\rm inv}$, $i_{\rm p}$, $V_{\rm bat}$, and $I_{\rm bat}$ for load-independent voltage mode for $R_{\rm bat} = 40\,\Omega$ under k_3 condition with $\alpha = 128°$ and $\alpha = 136°$, respectively. (upper) $\alpha = 128°$, and (lower) $\alpha = 136°$.

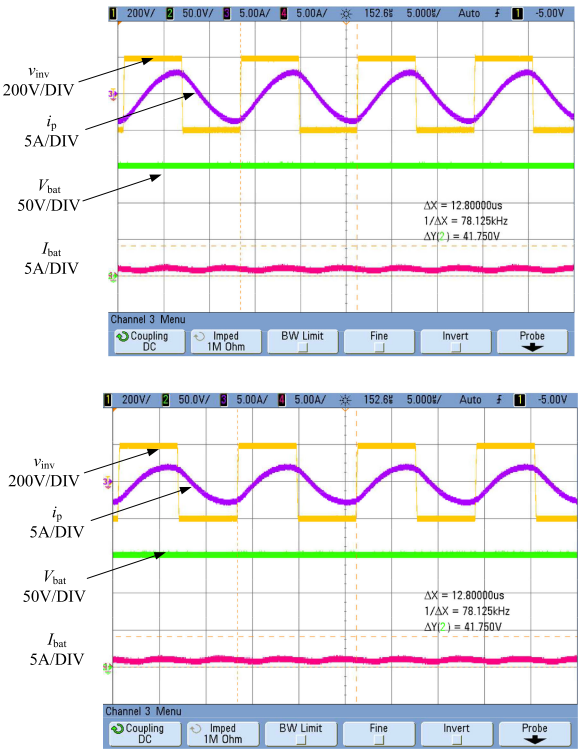

Fig. 23. Experimental waveforms of $v_{\rm inv}$, $i_{\rm p}$, $V_{\rm bat}$, and $I_{\rm bat}$ for load-independent voltage mode for $R_{\rm bat} = 135\,\Omega$ under k_3 condition with $\alpha = 128°$ and $\alpha = 136°$, respectively. (upper) $\alpha = 128°$, and (lower) $\alpha = 136°$.

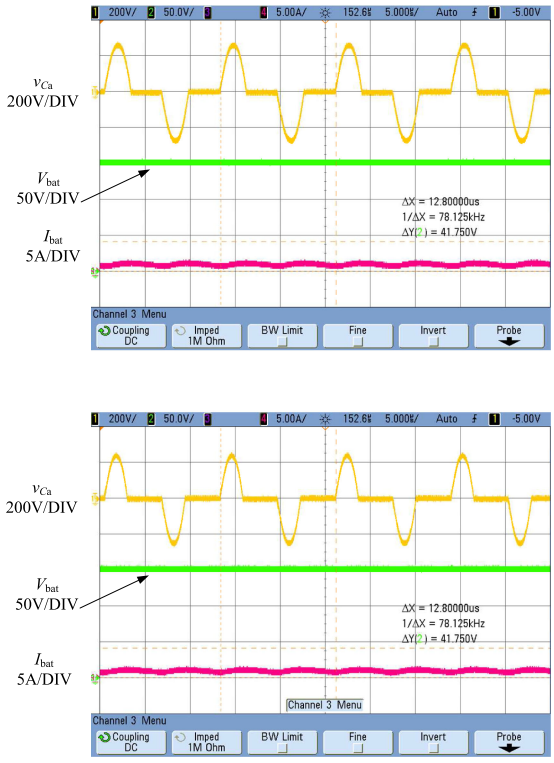

Fig. 24. Experimental waveforms of v_{Ca}, $V_{\rm bat}$, and $I_{\rm bat}$ for load-independent voltage mode for $R_{\rm bat} = 135\,\Omega$ under k_3 condition with $\alpha = 128°$ and $\alpha = 136°$, respectively. (upper) $\alpha = 128°$, and (lower) $\alpha = 136°$.

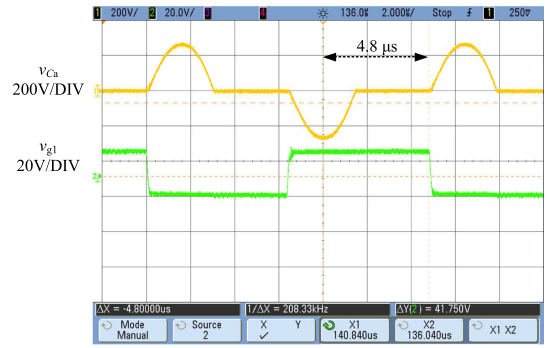

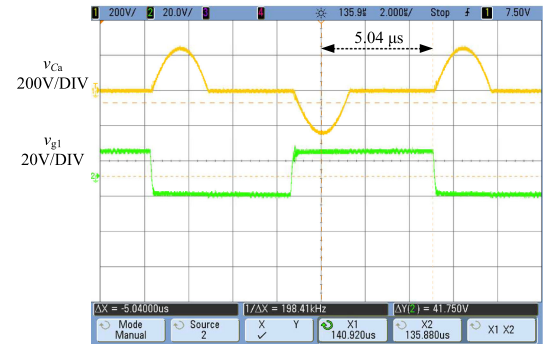

Fig. 25. Experimental waveforms of v_{Ca} and v_{g1} for load-independent voltage mode for $R_{\rm bat} = 135\,\Omega$ under k_3 condition with $\alpha = 128°$ and $\alpha = 136°$, respectively. (upper) $\alpha = 128°$, and (lower) $\alpha = 136°$.

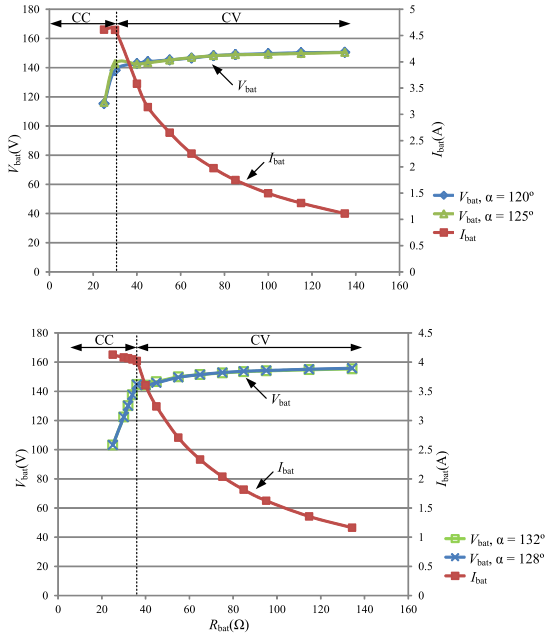

Fig. 26. Voltage and current variations of the dynamic S/SP compensated IPT converter under k_1 and k_3 conditions. (upper) k_1 condition, and (lower) k_3 condition.

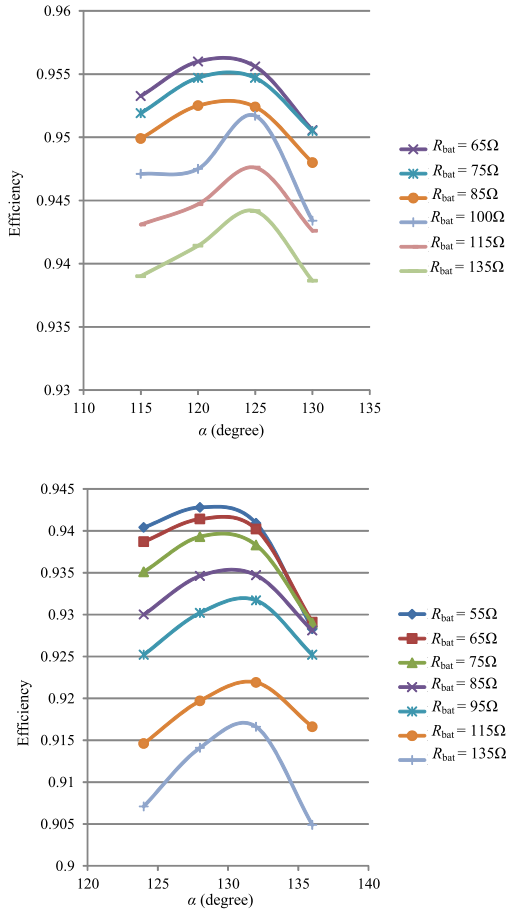

Fig. 27. Measured efficiencies of the proposed dynamic S/SP compensated IPT converter in the CV stage versus the effective value of C_3 under different $R_{\rm bat}$: (upper) k_1 condition and (lower) k_3 condition.

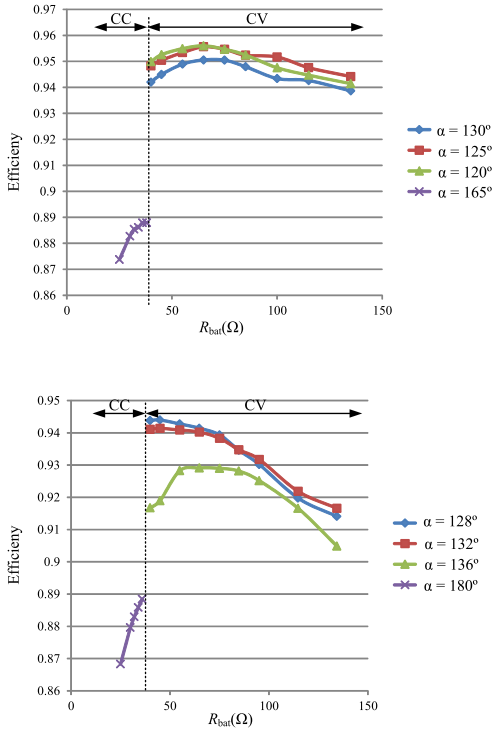

Fig. 28. Measured overall efficiencies of the proposed dynamic S/SP compensated IPT converter versus the effective value of $R_{\rm bat}$ under k_1 and k_3 conditions. (upper) k_1 condition, and (lower) k_3 condition.

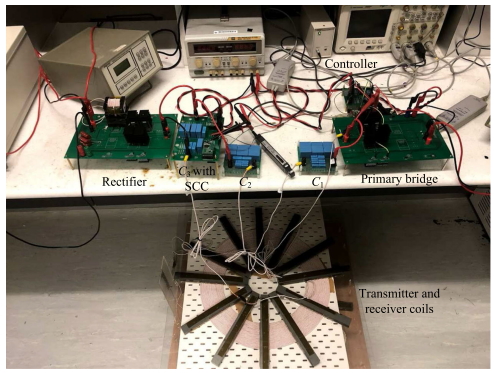

Fig. 29. Photograph of the experimental setup.

V. Conclusion

In this article, the work of the dynamic S/SP compensation network is further studied and its advantages are fully exploited for the development of CC–CV battery charger, which can retain all the desirable characteristics by programming the parameters of the compensation network under varying coupling condition. As inherited from the properties of the conventional S/S compensation counterpart, the dynamic S/SP compensation network also possesses load-independent voltage and current characteristics, which is favorable for the realization of ZVS, but with higher flexibility resulting from the extra control degree of freedom offered by the adjustable parallel compensation capacitance. With the aid of the SCC, the proposed network can flexibly

configure the charging current in the CC stage for different rates of charging process while the power transfer efficiency in the CV stage can be maximized without compromising the load-independent output voltage characteristic. In view of the addition of the SCC, the efficiency of the dynamic S/SP compensation network is analyzed and alternative design criterion for the effective parallel compensation capacitance in the CC and CV stages are suggested in this article. Finally, the design procedure is outlined and the design example is validated by experimental prototype.

REFERENCES

[1] C. T. Rim and C. Mi, *Wireless Power Transfer for Electric Vehicles and Mobile Devices*. Hoboken, NJ, USA: Wiley, 2017.

[2] B. Choi, J. Nho, H. Cha, T. Ahn, and S. Choi, "Design and implementation of low-profile contactless battery charger using planar printed circuit board windings as energy transfer device," *IEEE Trans. Ind. Electron.*, vol. 51, no. 1, pp. 140–147, Feb. 2004.

[3] Y. Jang and M. M. Jovanovic, "A contactless electrical energy transmission system for portable-telephone battery chargers," *IEEE Trans. Ind. Electron.*, vol. 50, no. 3, pp. 520–527, Jun. 2003.

[4] Z. Huang, S.-C. Wong, and C. K. Tse, "Design of a single-stage inductive-power-transfer converter for efficient EV battery charging," *IEEE Trans. Veh. Technol.*, vol. 66, no. 7, pp. 5808–5821, Jul. 2016.

[5] S. Li and C. C. Mi, "Wireless power transfer for electric vehicle applications," *IEEE J. Emerg. Sel. Topics Power Electron.*, vol. 3, no. 1, pp. 4–17, Mar. 2014.

[6] Q. Chen, S. C. Wong, C. K. Tse, and X. Ruan, "Analysis, design, and control of a transcutaneous power regulator for artificial hearts," *IEEE Trans. Biomed. Circuits Syst.*, vol. 3, no. 1, pp. 23–31, Feb. 2009.

[7] D. Ahn and S. Hong, "Wireless power transmission with self-regulated output voltage for biomedical implant," *IEEE Trans. Ind. Electron.*, vol. 61, no. 5, pp. 2225–2235, May 2013.

[8] Y. Gao, X. Zhang, Q. Cheng, B. Guo, and J. Yang, "Classification and review of the charging strategies for commercial lithium-ion batteries," *IEEE Access*, vol. 7, pp. 43511–43524, 2019.

[9] P. Keil and A. Jossen, "Charging protocols for lithium-ion batteries and their impact on cycle life-an experimental study with different 18650 high-power cells," *J. Energy Storage*, vol. 6, pp. 125–141, 2016.

[10] A. Ayachit and M. K. Kazimierczuk, "Transfer functions of a transformer at different values of coupling coefficient," *IET Circuits, Devices Syst.*, vol. 10, no. 4, pp. 337–348, Jul. 2016.

[11] X. Qu, Y. Jing, H. Han, S.-C. Wong, and C. K. Tse, "Higher order compensation for inductive-power-transfer converters with constant-voltage or constant-current output combating transformer parameter constraints," *IEEE Trans. Power Electron.*, vol. 32, no. 1, pp. 394–405, Jan. 2016.

[12] C.-S. Wang, G. A. Covic, and O. H. Stielau, "Power transfer capability and bifurcation phenomena of loosely coupled inductive power transfer systems," *IEEE Trans. Ind. Electron.*, vol. 51, no. 1, pp. 148–157, Feb. 2004.

[13] X. Qu, H. Han, S.-C. Wong, C. K. Tse, and W. Chen, "Hybrid IPT topologies with constant current or constant voltage output for battery charging applications," *IEEE Trans. Power Electron.*, vol. 30, no. 11, pp. 6329–6337, Nov. 2015.

[14] R. Mai, Y. Chen, Y. Li, Y. Zhang, G. Cao, and Z. He, "Inductive power transfer for massive electric bicycles charging based on hybrid topology switching with a single inverter," *IEEE Trans. Power Electron.*, vol. 32, no. 8, pp. 5897–5906, Aug. 2017.

[15] Y. Chen, B. Yang, Z. Kou, Z. He, G. Cao, and R. Mai, "Hybrid and reconfigurable IPT systems with high-misalignment tolerance for constant-current and constant-voltage battery charging," *IEEE Trans. Power Electron.*, vol. 33, no. 10, pp. 8259–8269, Oct. 2018.

[16] Y. Chen, Z. Kou, Y. Zhang, Z. He, R. Mai, and G. Cao, "Hybrid topology with configurable charge current and charge voltage output-based WPT charger for massive electric bicycles," *IEEE J. Emerg. Sel. Topics Power Electron.*, vol. 6, no. 3, pp. 1581–1594, Sep. 2018.

[17] U. K. Madawala and D. J. Thrimawithana, "A bidirectional inductive power interface for electric vehicles in V2G systems," *IEEE Trans. Ind. Electron.*, vol. 58, no. 10, pp. 4789–4796, Oct. 2011.

[18] S. Li, W. Li, J. Deng, T. D. Nguyen, and C. C. Mi, "A double-sided LCC compensation network and its tuning method for wireless power transfer," *IEEE Trans. Veh. Technol.*, vol. 64, no. 6, pp. 2261–2273, Jun. 2014.

[19] X. Qu, H. Chu, S.-C. Wong, and C. K. Tse, "An IPT battery charger with near unity power factor and load-independent constant output combating design constraints of input voltage and transformer parameters," *IEEE Trans. Power Electron.*, vol. 34, no. 8, pp. 7719–7727, Aug. 2019.

[20] L. Yang, X. Li, S. Liu, Z. Xu, and C. Cai, "Analysis and design of an LCCC/S compensated WPT system with constant output characteristics for battery charging applications," *IEEE J. Emerg. Sel. Topics Power Electron*., vol. 9, no. 1, pp. 1169–1180, Feb. 2021.

[21] J. Lu, G. Zhu, D. Lin, S.-C. Wong, and J. Jiang, "Load-independent voltage and current transfer characteristics of high-order resonant network in IPT system," *IEEE Trans. Emerg. Sel. Topics Power Electron.*, vol. 7, no. 1, pp. 422–436, Mar. 2019.

[22] E. Gati, G. Kampitsis, and S. Manias, "Variable frequency controller for inductive power transfer in dynamic conditions," *IEEE Trans. Power Electron.*, vol. 32, no. 2, pp. 1684–1696, Feb. 2016.

[23] L. Xu, Q. Chen, X. Ren, S.-C. Wong, and C. K. Tse, "Self-oscillating resonant converter with contactless power transfer and integrated current sensing transformer," *IEEE Trans. Power Electron.*, vol. 32, no. 6, pp. 4839–4851, Jun. 2016.

[24] A. Koran and K. Badran, "Adaptive frequency control of a sensorless-receiver inductive wireless power transfer system based on mixed-compensation topology," *IEEE Trans. Power Electron.*, vol. 36, no. 1, pp. 978–990, Jan. 2021.

[25] Y. Jiang, L. Wang, J. Fang, C. Zhao, K. Wang, and Y. Wang, "A joint control with variable ZVS angles for dynamic efficiency optimization in wireless power transfer system," *IEEE Trans. Power Electron.*, vol. 35, no. 10, pp. 11064–11081, Oct. 2020.

[26] Y. Jiang, L. Wang, Y. Wang, J. Liu, M. Wu, and G. Ning, "Analysis, design, and implementation of WPT system for EV's battery charging based on optimal operation frequency range," *IEEE Trans. Power Electron.*, vol. 34, no. 7, pp. 6890–6905, Jul. 2019.

[27] J. Hou, Q. Chen, S.-C. Wong, C. K. Tse, and X. Ruan, "Analysis and control of series/series-parallel compensated resonant converter for contactless power transfer," *IEEE J. Emerg. Sel. Topics Power Electron.*, vol. 3, no. 1, pp. 124–136, Mar. 2014.

[28] J. Hou, Q. Chen, X. Ren, X. Ruan, S.-C. Wong, and C. K. Tse, "Precise characteristics analysis of series/series-parallel compensated contactless resonant converter," *IEEE J. Emerg. Sel. Topics Power Electron.*, vol. 3, no. 1, pp. 101–110, Mar. 2014.

[29] C. S. Wong, Y. P. Chan, L. Cao, L. Wang, K. H. Loo, and M. C. Wong, "A single-stage dynamically compensated IPT converter with unity power factor and constant output voltage under varying coupling condition," *IEEE Trans. Power Electron.*, vol. 35, no. 10, pp. 10121–10136, Oct. 2020.

[30] X. Wang, J. Xu, M. Leng, H. Ma, and S. He, "A hybrid control strategy of LCC-S compensated WPT system for wide output voltage and ZVS range with minimized reactive current," *IEEE Trans. Ind. Electron*., to be published.

[31] X. Wang, J. Xu, H. Ma, and S. He, "Inductive power transfer systems with digital switch-controlled capacitor for maximum efficiency point tracking," *IEEE Trans. Ind. Electron*., to be published.

[32] J. Zhang, J. Zhao, Y. Zhang, and F. Deng, "A wireless power transfer system with dual switch-controlled capacitors for efficiency optimization," *IEEE Trans. Power Electron.*, vol. 35, no. 6, pp. 6091–6101, Jun. 2020.

[33] A. Ayachit, F. Corti, A. Reatti, and M. K. Kazimierczuk, "Zero-voltage switching operation of transformer class-e inverter at any coupling coefficient," *IEEE Trans. Ind. Electron.*, vol. 66, no. 3, pp. 1809–1819, Mar. 2019.

[34] J. Lu, G. Zhu, D. Lin, Y. Zhang, H. Wang, and C. C. Mi, "Realizing constant current and constant voltage outputs and input zero phase angle of wireless power transfer systems with minimum component counts," *IEEE Trans. Intell. Transp. Syst.*, vol. 22, no. 1, pp. 600–610, Jan. 2021.

[35] S. TIR, Wireless Power Transfer for Light-Duty Plug-In/Electric Vehicles and Alignment Methodology, SAE J2954, 2016.

[36] Y. P. Chan, C. S. Wong, and K. H. Loo, "Dual-mode modulation scheme with seamless transition for a tunable immittance-based DAB converter featuring high-efficiency performance over whole output power range," *IEEE Trans. Power Electron.*, vol. 35, no. 9, pp. 9184–9201, Sep. 2020.

[37] C. S. Wong *et al.*, "Independent control of multicolor-multistring LED lighting systems with fully switched-capacitor-controlled LCC resonant network," *IEEE Trans. Power Electron.*, vol. 33, no. 5, pp. 4293–4305, May 2017.

[38] S. Kim, G. A. Covic, and J. T. Boys, "Tripolar pad for inductive power transfer systems for EV charging," *IEEE Trans. Power Electron.*, vol. 32, no. 7, pp. 5045–5057, Jul. 2016.

[39] X. Qu, Y. Jing, J. Lian, S.-C. Wong, and C. K. Tse, "Design for continuous-current-mode operation of inductive-power-transfer converters with load-independent output," *IET Power Electron.*, vol. 12, no. 10, pp. 2458–2465, 2019.

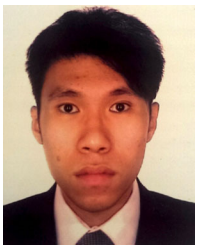

Chi Shing Wong (Member, IEEE) received the B.Eng. (hons.) degree in electronic and information engineering and the Ph.D. degree in power electronics from The Hong Kong Polytechnic University, Hong Kong, in 2013 and 2018, respectively.

He was a Visiting Scholar with the School of Electrical, Electronic and Computer Engineering, University of Western Australia, Perth, WA, Australia, from January 2017 to May 2017. From 2019 to 2020, he was a Postdoctoral Fellow with The State Key Laboratory of Internet of Things for Smart City, University of Macau, Macao, China, under the UM Macao Talent Program. He is currently with the Department of Electronic and Information Engineering, The Hong Kong Polytechnic University, under the Hong Kong RGC Postdoctoral Fellowship Scheme. His research interests include solid-state transformer, inductive power transfer, vehicle-to-grid (V2G), LED driver circuit design, power-factor-correction regulators, and resonant power conversion.

Dr. Wong is currently a reviewer for various international journals and conferences.

Man-Chung Wong (Senior Member, IEEE) received the B.Sc. and M.Sc. degrees in electrical and electronics engineering from the University of Macau (UM), Macao, China, and the Ph.D. degree from the Department of Electrical Engineering, Tsinghua University, Beijing, China.

He is currently a Professor with the Department of Electrical and Computer Engineering, UM. He was a Visiting Fellow with Cambridge University, Cambridge, U.K., and is currently with the State Key Laboratory of Internet of Thing Smart City and Sate Key Laboratory of Analog and Mixed Signal VLSI, UM. He has authored or coauthored four books and more than 150 technical journals and conference papers. He holds four U.S. patent and eight Chinese patents. Since 2017, he has been with the Department Head of Electrical and Computer Engineering, FST, UM. His research interests include integrated power electronics controllers, power electronics converters, power quality compensators, renewable energy, wireless power transfer and smart grid.

Prof. Wong was a recipient of Macao Science and Technology Invention Awards (Second Class at 2018, Third Class at 2014 and 2012, respectively) and Yong Scientist Award from "Insituto Internacional De Macau" at 2000, Young Scholar Award form UM at 2001, and Second Prize of 2003 Tsinghua University Excellent Doctor Thesis Award. He was the IEEE TENCON Macao 2015 General Chair and IEEE APPEEC Macao 2019 General Chair. He was the Chair of IEEE Macau Section at 2014–2015. He is currently the Chair of IEEE Macau PES/PELS Joint Chapter and IEEE Region 10 Power and Energy Society North Representative since 2015.

Lingling Cao (Member, IEEE) received the B.S. and M.S. degrees in electrical engineering from the Nanjing University of Aeronautics and Astronautics, Nanjing, China, in 2008 and 2011, and the Ph.D. degree from the Hong Kong Polytechnic University, Hong Kong, in 2015.

She is currently an Assistant Professor with the Harbin Institute of Technology, Shenzhen, China. Her research interests include power converters for renewable energy systems and wireless power transfer technologies.

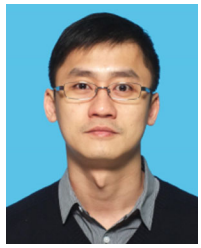

K. H. Loo (Member, IEEE) received the B.Eng. (hons.) in electronic engineering and the Ph.D. degree from the University of Sheffield, Sheffield, U.K., in 1999 and 2002, respectively.

He was a Postdoctoral Researcher with the Ehime University, Matsuyama, Japan, from 2002 to 2004. In 2006, he joined The Hong Kong Polytechnic University where he is currently an Associate Professor with the Department of Electronic and Information Engineering. His research interests include high-frequency power conversion, in particular power converters for renewable energy systems.

Dr. Loo has been an Associate Editor for the IEEE TRANSACTIONS ON ENERGY CONVERSION since 2013 and IEEE POWER ENGINEERING LETTERS since 2015, and contributes regularly as a reviewer for various international journals and conferences. He is currently the Chair of the Power Electronics and Control Sub-Committee of the IEEE Technical Committee on Transportation Electrification. Upon completion of his doctoral degree, he was the recipient of the Japan Society for the Promotion of Science (JSPS) Postdoctoral Fellowship.